Reconstruction of decays of strange particles produced in Xe+CsI interactions with the BM@N detector

Roman Zinchenko[1], Julieta Drnoyan[1], Mikhail Kapishin[1], Igor Roufanov[1], Veronika Vasendina[1], Alexander Zinchenko ⓘ *,[1], and Dmitry Zinchenko[1]

[1]Joint Institute for Nuclear Research, Joliot-Curie 6, Dubna 141980, Moscow region, Russia

February 9, 2025

Abstract

In December, 2022 - January, 2023 the BM@N experiment conducted its first physics run with full detector configuration. Over 500 million events of Xe+CsI interactions with the Xe beam kinetic energy of 3.8A GeV were collected.

Since then, strong efforts have been put to reconstruct the collected data and make preparations for physics analyses. The current status of such an activity related to reconstruction of strange particles weakly decayed to charged hadrons is presented in this paper. Main steps of the analysis procedure for a study of the strangeness production are outlined as well.

Реконструкция распадов странных частиц, рождённых во взаимодействиях Xe+CsI, в детекторе BM@N

Р.А. Зинченко, Д.Р. Дрноян, М.Н. Капишин, И.А. Руфанов, В.А. Васендина, А.И. Зинченко, Д.А. Зинченко

*E-mail: Alexander.Zinchenko@jinr.ru

1   Introduction

The experimental study of nuclear collisions in the energy range of several GeV per nucleon provides new information on the quantum chromodynamic (QCD) phase diagram at large baryon-chemical potentials, including the high-density equation-of-state (EOS) [1–4]. This is the main research subject of several ongoing and future experiments [5].

The Baryonic Matter at the Nuclotron (BM@N) at the NICA complex is one of such experiments. It carries out measurements with heavy ions at collision energies of $\sqrt{s_{NN}}$ = 2.3 - 3.3 GeV , where the highest net-baryon densities is created. In the last few years, the experiment performed several technical runs with light ions in partial detector configuration [6, 7]. The results obtained served as a proof of the detector concept, data processing and event reconstruction approaches. With the Booster startup at the end of 2020, the accelerator complex of the Booster and Nuclotron at JINR became capable of accelerating heavy-ion beams. The first physics run at the BM@N setup with Xe beam was performed in December, 2022 - January, 2023. Over 500 million events of Xe+CsI interactions with the Xe beam kinetic energy of 3.8A GeV ($\sqrt{s_{NN}}$ = 3.263 GeV) were collected.

Since then, the BM@N Colaboration worked hard to reconstruct the experimental data and properly tune the Monte Carlo simulation codes, i.e. to prepare for physics analyses on several topics. One of the most important items of the experimental program is a study of the strangeness production in nuclear collisions [8]. The current status of the activity in this research domain is presented in this paper. It demonstrates the detector performance for reconstruction of strange particle decays as well as shows the ability of the experiment to extract relevant physics observables, outlining the direction and steps of upcoming data analysis.

2   BM@N detector configuration

The layout of the BM@N setup in Xe+CsI run is presented in Fig. 1. Tracks of charged particles are reconstructed with the hybrid tracking system consisting of 4 stations of double-sided microstrip silicon sensors (Forward Silicon Detector) downstream from the single-layer target, located inside the Barrel Detector, and a set of 7 planes of GEM (gaseous electron multiplier) detectors with two-coordinate strip readout mounted downstream from the silicon stations. The Forward Silicon subsystem contains 6, 10, 14 and 18 detector modules in stations 1-4, respectively, arranged into pairs of half-stations below and above the beam line at a distance of $\sim$10 cm between stations. Each module with a width of 6 and a height of 12 cm (9 cm in the first station) has a strip pitch of 100 μm and a stereo angle, i.e. angle between strips on different sides, of 2.5°. The GEM detectors with a strip pitch of 800 μm and a stereo angle of 15° cover the region of $\pm \sim$80 and $\pm \sim$40 cm in horizontal (X-axis) and vertical (Y-axis) directions, respectively, and positioned at a distance of $\sim$30 cm from each other along the beam (Z-axis) below and above the beam pipe. Both the Forward Silicon and the GEM stations are installed inside a large aperture dipole magnet with a gap height of 1 m, providing a vertical magnetic field of up to 1.0 T in the magnet center. For different incoming beam rigidities, the magnetic field value is adjusted to steer the non-interacting beam particles through the vacuum beam pipe. For particle identification, the particle time-of-flight is measured with 2 walls of resistive plate chambers (mRPC) with strip readout, located at $\sim$4 m (TOF400) and $\sim$7 m (TOF700) downstream from the target. The Cathode Strip Chambers improve quality of spatial matching of reconstructed tracks with TOF measurements. The interaction centrality and event plane are characterized with the Forward Hadron Calorimeter. The interaction trigger is produced with the Barrel Detector, surrounding the target. More details on the BM@N detector systems can be found in Ref. [9].
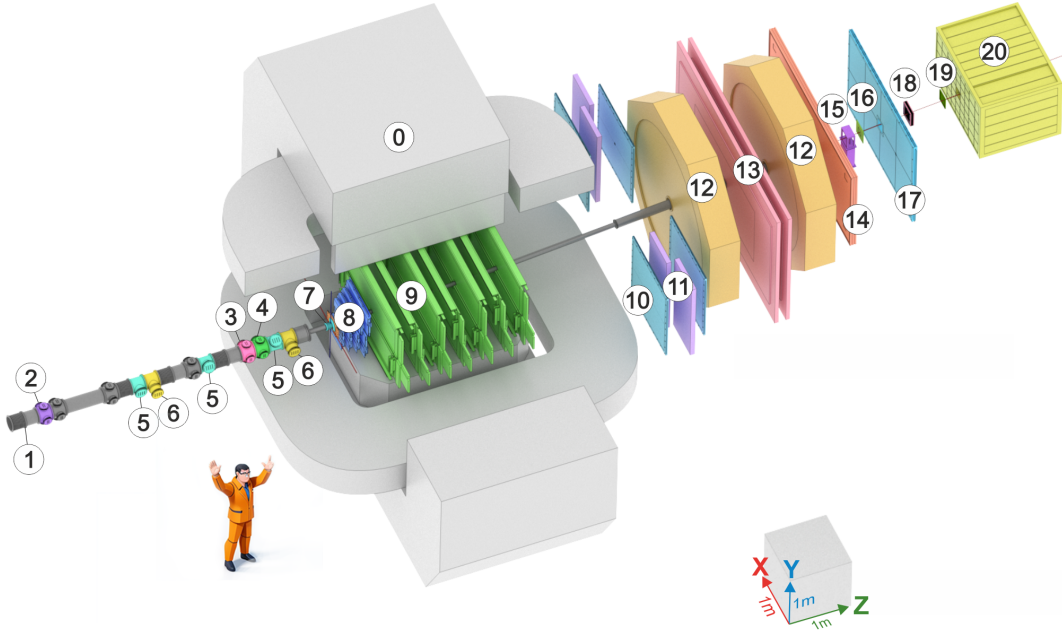
Figure 1: Three-dimensional view of the BM@N setup. 0) SP-41 analyzing magnet. 1) Vacuum beam pipe. 2) BC1 beam counter. 3) Veto counter. 4) BC2 beam counter. 5) Silicon Beam Tracker. 6) Silicon beam profilometers. 7) Barrel Detector. 8) Forward Silicon Detector. 9) Gaseous Electron Multiplier (GEM) detectors. 10) Small cathode strip chambers. 11) TOF400 system. 12) Drift chambers. 13) TOF700 system. 14) Scintillation Wall. 15) Fragment Detector. 16) Small GEM detector. 17) Large cathode strip chamber. 18) Gas ionization chamber as beam profilometer. 19) Forward Quartz Hodoscope. 20) Forward Hadron Calorimeter. The ion beam comes from the left through the vacuum beam pipe to avoid interactions with the air. Target is located inside the Barrel Detector (7).

3   Event reconstruction

For track reconstruction, a so-called Vector Finder toolkit [10, 11], implemented within the BmnRoot software framework [12], is used. It realizes a constrained combinatorial search for combinations of detector hits which can be potentially produced by the same particle. Track candidates found are fitted with a Kalman filter procedure.

The reconstructed tracks are used to find the primary (interaction) vertex. The vertex-fitting procedure is based on the Kalman filtering technique [13]. A similar Kalman-based approach is used in the decay reconstruction package, i.e. to find secondary (decay) vertices [14, 15].

Strange particles can be reconstructed from their weak decays to charged particles in the final state. Such decays create quite clear event topologies, as can be seen in Fig. 2, where a schematic view of one of such topologies, namely, a two-prong decay of a neutral particle (so-called "V0-decay"), is shown in the bending plane of the magnet, i.e. in the plane perpendicular to the magnetic field.

Such topologies can be identified using the secondary vertex reconstruction technique, which is based on selecting track combinations producing secondary (decay) vertices decoupled from the primary one (interaction point). The selection strength is controlled by applying different criteria on relevant kinematic and topological variables. For example, track combinations are accepted only if the

distance of the closest approach dca_{V0} in space between daughter tracks is smaller than some upper cut value. This cut ensures that the tracks originate from the same mother particle. To select decays of relatively long-lived particles, it is commonly required that the secondary vertex position is located farther than some lower cut distance *path* from the primary one. In order to suppress the combinatorial background produced by primary tracks, the minimum value of the daughter track impact parameters to the primary vertex $dca_{p,\pi}$ should exceed some threshold. The quality of the decay reconstruction can be further improved by requiring the impact parameter of the decayed particle with respect to the primary vertex or its pointing angle, defined as the angle between its momentum and the direction vector from the primary to the secondary vertex, to be smaller than some value. The *DCA*-cuts can be also used normalized to their errors, i.e. expressed as their respective χ^2-values. In this way, it is possible to take into account the *DCA*-dependence on the transverse momentum, for example, and, therefore, to increase the selection power. In addition, to reject some fake tracks it can be useful to apply some minimum momentum or transverse momentum p_T cut.

For selected particle combinations, the invariant mass is calculated under the corresponding daughter particle hypotheses. Since, for this study, particle identification based on the TOF system is not used, the daughter particles are assumed to be a proton and a negative pion for the case of Λ hyperon and negative and positive pions for K_S^0 meson reconstruction. Observation of clear peaks in the invariant mass distributions at the right particle mass values serves as a clear signature of the strange particle decays under study.
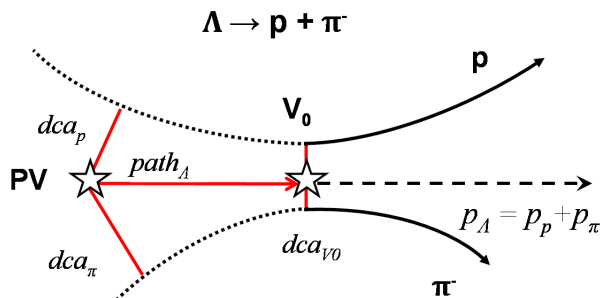

Figure 2: View of the Λ hyperon decay topology ($\to p + \pi^-$) in the bending plane of the magnetic field. Here, dca_p and dca_π are the distances of the closest approach (DCA) of the decay tracks to the primary vertex PV; dca_{V0} is the distance between daughter tracks in the mother decay vertex V_0; *path* is the mother particle decay length, and $\mathbf{p}_p$, $\mathbf{p}_\pi$ and $\mathbf{p}_\Lambda$ are momenta of particles.

4 Λ hyperon and K_S^0 meson reconstruction results

Figure 3 shows invariant mass distributions of Λ and K_S^0 candidates after applying selection criteria, explained in the previous section. The exact values of the cuts are presented in Table 1. They were found from a multidimensional scan over parameter values. For each set of values the peak significance was calculated and the final result corresponds to its maximum. The significance is defined as $S/\sqrt{S+B}$, where S and B are the signal and background contributions inside some interval around the peak position, i.e. $S+B$ is the full integral of the invariant mass distribution over the interval width and S is the integral value after the background subtraction. The background contribution in the peak region can be estimated using either the polynomial fit outside it or the event mixing technique [16].

Having selected strange particle signal, the next step to proceed is to extract physics observables useful for comparison with other experiments and theoretical models. For this, first of all, it is nec-

essary to check the consistency of selection cuts in experimental and simulated data. It can be done by looking at the particle yield versus one of the selection variables while keeping the others at their nominal value. As can be seen in Fig. 4, the experimental and simulated results agree quite well, the residual difference is not essential for this study and can be taken into account in future analyses. Then the experimentally measured distributions should be corrected for the total detector efficiency. It is estimated from detector simulation and combines geometric efficiency (acceptance), efficiency of the tracking detectors and reconstruction efficiency. The validity of the efficiency estimates can be checked from some inclusive distributions (e.g., number of hits per reconstructed track), or from a reference (model - independent) process if possible. For strange particles under study, such a process is their weak decay. The obtained results on the lifetime measurement of Λ hyperons and K_S^0 mesons are presented below along with some additional very preliminary results on strange particle production properties in Xe+CsI interactions, which better illustrate the reconstruction performance and should be considered as some validation steps toward physics analyses. The results presented were obtained for 5 million recorded triggers and 2 million Monte Carlo simulated events. This event statistics defines the errors shown in all the plots below. No systematic effects have been estimated at this stage.
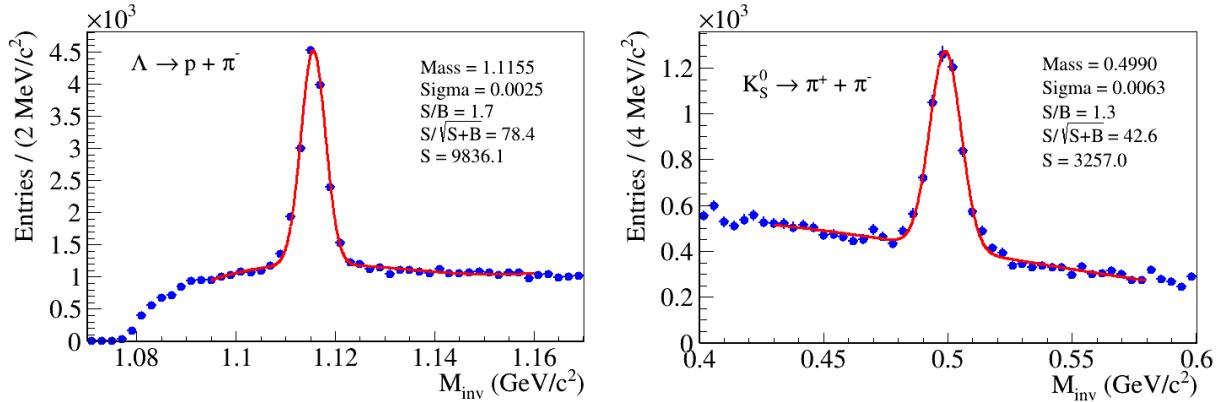

Figure 3: Invariant mass distributions of Λ (left) and K_S^0 (right) candidates for 1 million collected events. The histograms are fitted by a sum of a gaussian and a 3-rd degree polynomial functions. The gaussian function is used to define the signal interval as $\pm 2.5\sigma$ around the peak position, while the polynomial function is used to evaluate the background under the peak. The numbers in the legend show the peak position and σ of the gaussian function, signal-to-background ratio, significance and signal contribution inside the signal interval.

Table 1: Selection criteria used for Λ and K_S^0 reconstruction. Cuts on DCAs are imposed in the χ^2-space, i.e., after normalization to respective parameter errors.

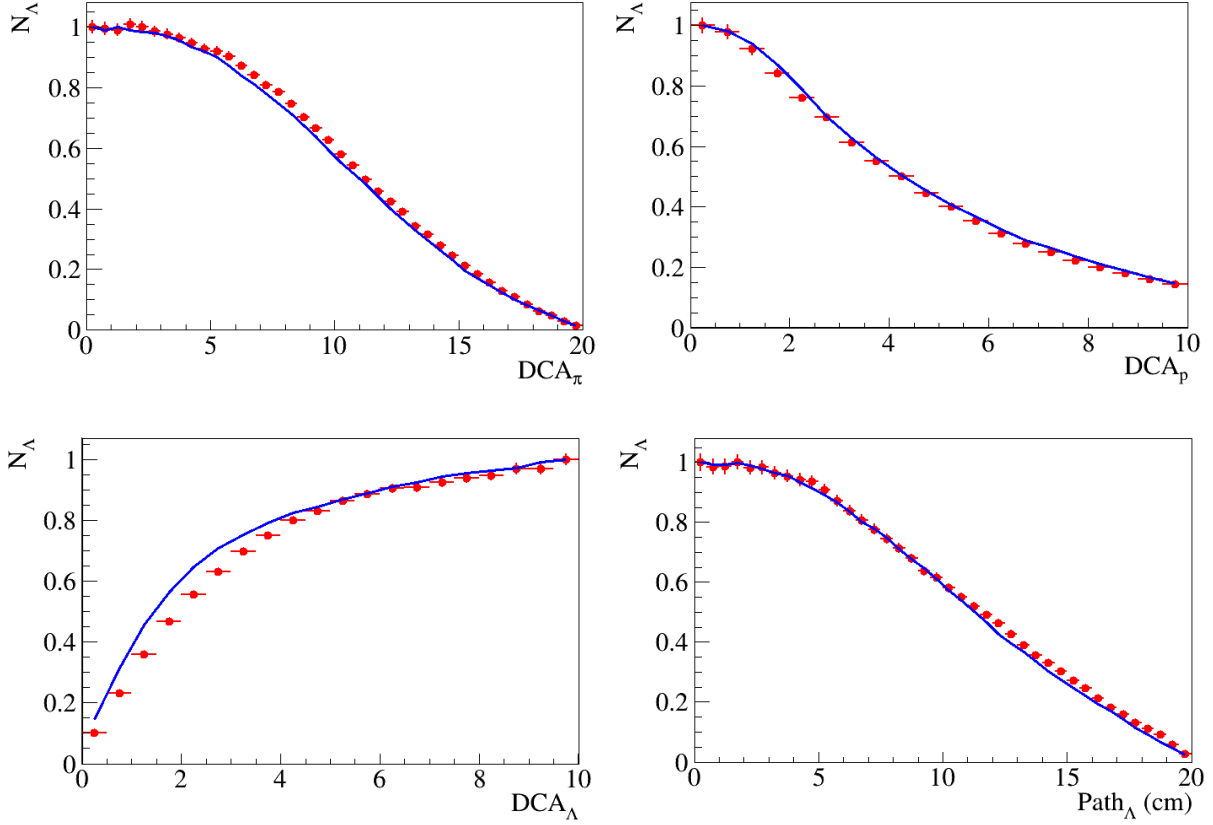| Cut	Λ	K_S^0
DCA of daughters to primary vertex	$> 6.0(\pi), > 3.3(p)$	$> 5.8(\pi^+, \pi^-)$
DCA of mother to primary vertex	<4.3	<5.0
Decay length, cm	>5.2	>2.3
p_T, GeV/c	$> 0.05(\pi), > 0.1(p)$	$> 0.1(\pi^+, \pi^-)$

Figure 4: Λ hyperon reconstructed yield versus different selection cuts. The other variables are set to their nominal values (see Table 1). Histograms are normalized to their values either at 0 or at the right edge. Red symbols represent experimental data, blue lines simulated ones.

4.1 Λ hyperon

To illustrate the efficiency effect on the decay curve, Fig. 5 shows the decay time (lifetime) distribution of all Λ hyperons produced by the Monte Carlo event generator DCM-SMM [17] and the ones after detector simulation, event reconstruction and decay selection procedures presented above. The distortion is quite visible. The lifetime t is calculated according to the formula

$$t = L \cdot m_0/(p \cdot c), \tag{1}$$

where L is the decay length, m_0 and p are the mass and momentum of the particle and c is the speed of light. The decay time distribution is described by the formula

$$dN/dt = N_0/\tau \cdot \exp(-t/\tau), \tag{2}$$

where N_0 is the total number of particles and τ is the mean lifetime. The original decay curve can be reconstructed from measurements in several lifetime intervals (e.g., in 9 lifetime bins, shown on the right plot of Fig. 5). Figures 6 and 7 illustrate the sequence of the steps of the decay curve reconstruction procedure which consists in the following. Λ hyperon invariant mass distribution is built for each lifetime interval (Fig. 6left). After background subtraction (Fig. 6right), the yield is calculated as the number of counts in the peak region, i.e. within $\pm 2.5\sigma$ around the invariant mass peak maximum position. This means that the gaussian peak fit is used only to define the signal region

and not to extract the particle yield, since the gaussian fit does not take into account possible distortion of the peak shape. These sums of histogram counts give the raw (uncorrected) lifetime distribution (Fig. 7left). The statistical errors shown are calculated as

$$\Delta S = \sqrt{T + B}, \tag{3}$$

where ΔS is the extracted signal error, T is the total histogram counts (before background subtraction) in the peak region and B is the background estimate. The total reconstruction efficiency is estimated from the Monte Carlo simulation (Fig. 7right) and defined as a ratio of fully reconstructed hyperons after final selection cuts to the ones produced in the full phasespace (and within 30 cm from the interaction point to reject hyperons created in the detector material). The efficiency is used to correct the raw distribution and extract the original one (Fig. 7bottom).
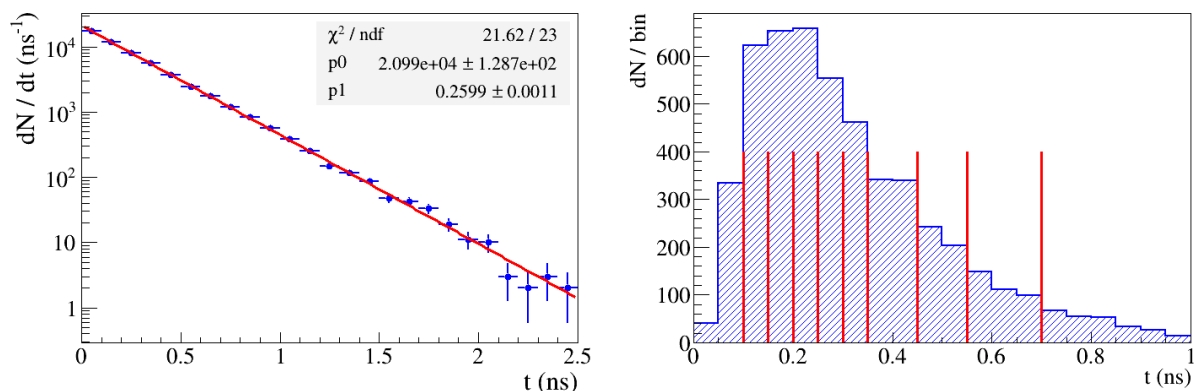
Figure 5: (Left) lifetime distribution of all generated Λ hyperons fitted to the decay curve given by formula (2) with $p1$ being the mean lifetime τ (the table value of 0.263 ns). (Right) lifetime distribution after detector simulation, event reconstruction and decay selection procedures. Vertical lines represent time intervals which were used to reconstruct the decay curve.
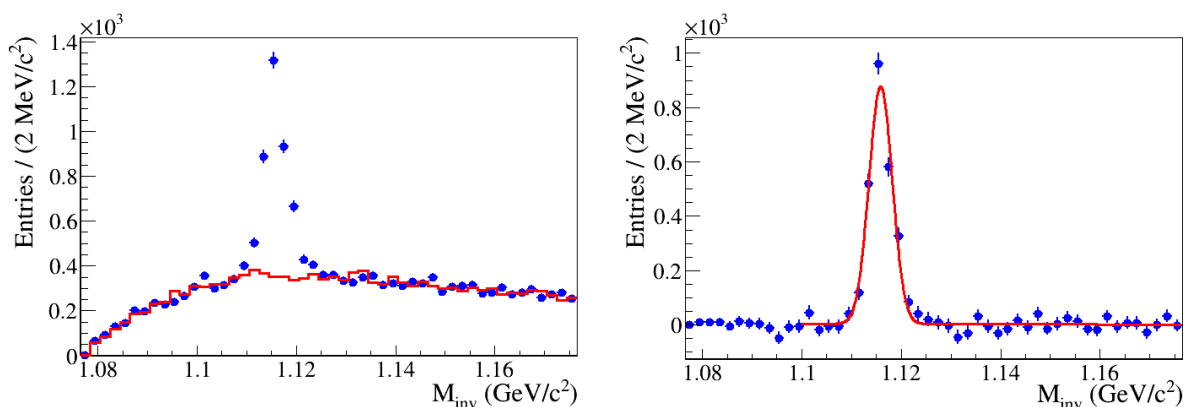

Figure 6: Invariant mass distributions of Λ candidates for the decay time bin of 0.1 - 0.2 ns before (left) and after (right) background subtraction.

Transverse momentum spectra of particles provide important information about physics processes during nucleus - nucleus interactions. For practical purposes, the transverse momentum p_T is often substituted by the transverse mass $m_T \equiv \sqrt{(p_T^2 + m_0^2)}$, where m_0 is the particle mass. Transverse
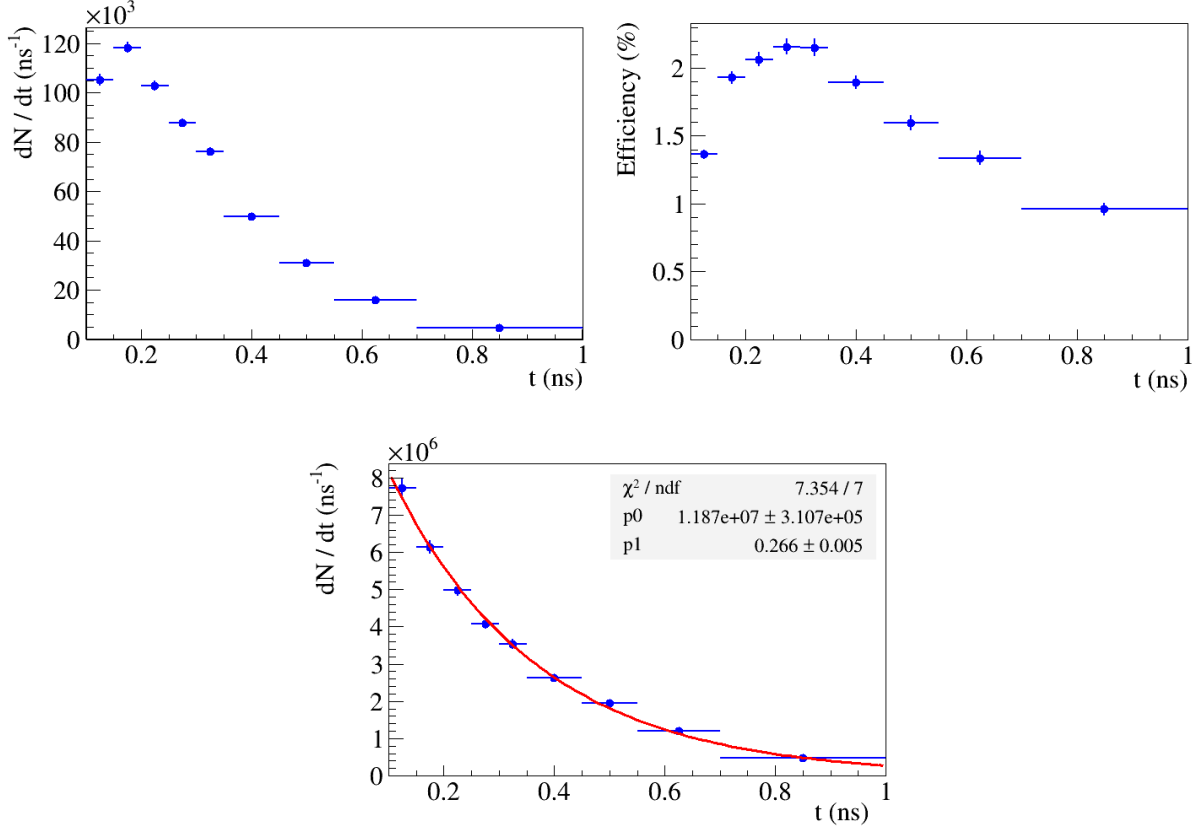
Figure 7: (Left) reconstructed Λ hyperon yield versus lifetime; (right) total Λ hyperon efficiency obtained from Monte Carlo simulation; (bottom) Λ hyperon lifetime distribution corrected for efficiency, fitted to the decay curve (2).

mass spectra can be obtained following the procedure similar to the one described above, i.e. obtaining particle yields from background-subtracted invariant mass spectra in bins of m_T and correcting for reconstruction efficiency. Validity of the efficiency estimates can be verified again from the reconstructed decay curve obtained from hyperon yields in lifetime intervals, where the yields are found from the corrected for efficiency m_T spectra for those lifetime bins. Thus, the procedure is based on a double - differential analysis, i.e. invariant mass distributions similar to Fig. 6 are constructed for two - dimensional $m_T - t$ bins. Then the raw m_T spectra (Fig. 8left) are corrected for the efficiency (Fig. 8right) defined as in the previous case but for the intervals of the lifetime. The corrected scaled m_T spectra, i.e. $1/m_T^2 \cdot dN/dm_T$, are fitted to the Boltzman expression [18]:

$$\frac{1}{m_T^2}\frac{dN}{dm_T} = C(t) \cdot \exp\left(-\frac{m_T - m_0}{T_{eff}}\right), \tag{4}$$

where $C(t)$ is the normalization constant and T_{eff} is the effective temperature. The fitting functions (Fig. 9left and right) are used to integrate dN/dm_T spectra and to obtain hyperon yields for the lifetime intervals (Fig. 9bottom). The integration over m_T is done as follows:

$$N(t) = \int_0^\infty \frac{dN}{dm_T}dm_T = C(t)\int_0^\infty m_T^2 \cdot \exp\left(-\frac{m_T - m_0}{T_{eff}}\right)dm_T =$$

$$C(t) \cdot \left(2T_{eff}^3 + 2T_{eff}^2 m_0 + T_{eff}m_0^2\right). \tag{5}$$

8

The resulting lifetime distribution is well fitted to the decay curve with a reasonable value of the mean lifetime. The obtained values of T_{eff} for different lifetime bins are close to each other as can be expected from the fact, that particle lifetime is not a variable which selects a particular region of the phasespace characterized by the effective temperature.
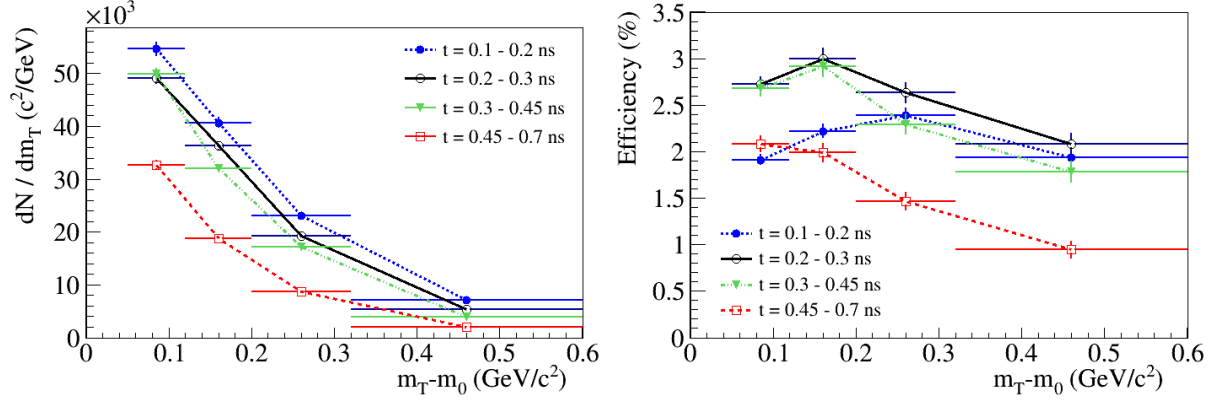

Figure 8: (Left) Λ hyperon raw yields versus transverse mass for 4 intervals of lifetime; (right) total reconstruction efficiency versus m_T for 4 lifetime intervals. Lines are drawn to guide the eye.

The next step toward physics analyses is reconstruction of particle m_T spectra in different rapidity y intervals. This can be done by extracting particle yields in 2-dimensional bins of $m_T - y$ and correcting for the total efficiency similar to the procedure described above. Results are illustrated in Figs. 10, 11 for 4 intervals of the proton-proton centre-of-mass rapidity $y_{cm} = y - 1.17$. Figure 11 includes also the model prediction from the DCM-SMM generator which is quite consistent with current test measurement. To make more fair comparison, dN/dy is calculated for experimental and simulated events where a primary vertex was reconstructed with at least two tracks. Such an event selection partially takes into account trigger conditions in the experiment (but, presumably, not completely). From the fits one can also see obvious rapidity dependence of the effective temperature T_{eff} and the trend is similar to previously observed in nuclear collisions [18].
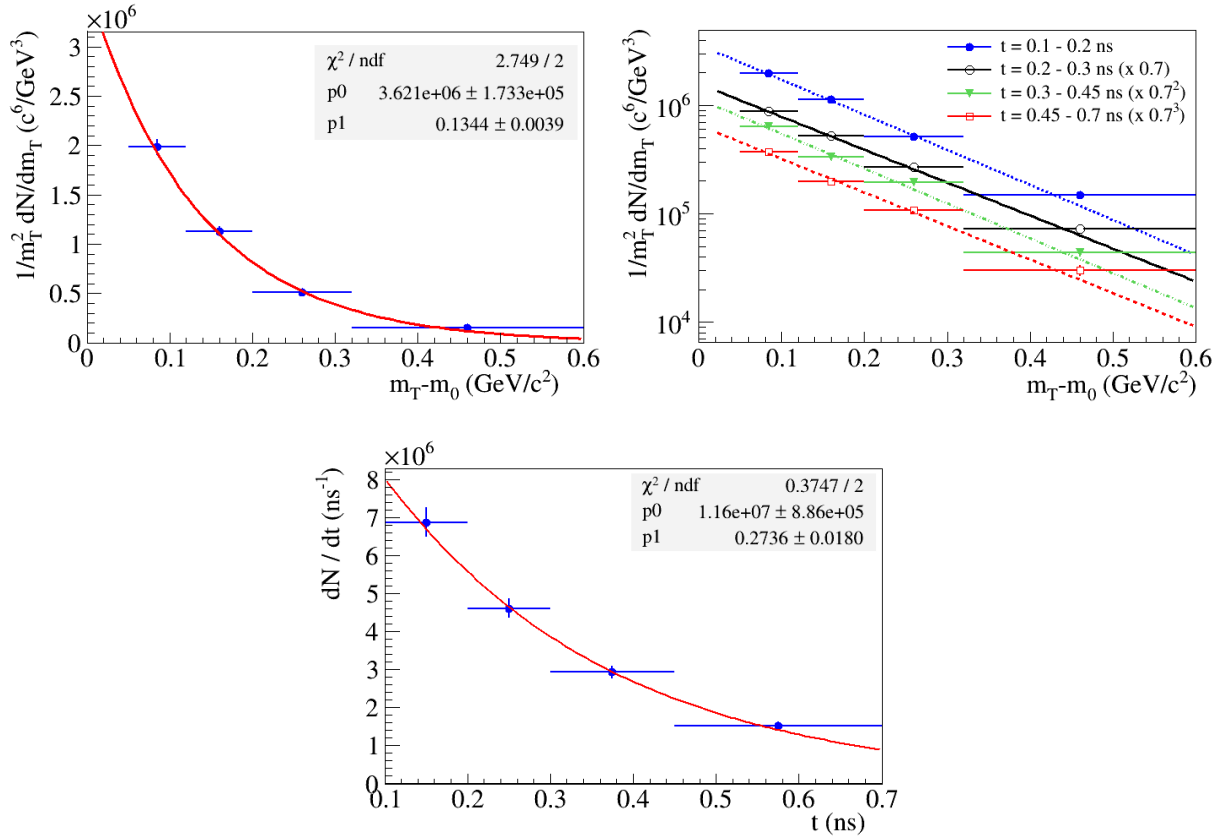
9

Figure 9: (Left) corrected for efficiency transverse mass distribution of Λ hyperons for the lifetime bin of 0.1 - 0.2 ns fitted to the Boltzman expression (4); (right) the same for 4 lifetime bins. The effective temperatures T_{eff} obtained are: 134±4, 143±4, 135±4 and 140±7 MeV for the lifetime bins of 0.1 - 0.2, 0.2 - 0.3, 0.3 - 0.45 and 0.45 - 0.7 ns, respectively. (Bottom) reconstructed decay curve from integrated m_T spectra fitted to the expression (2).
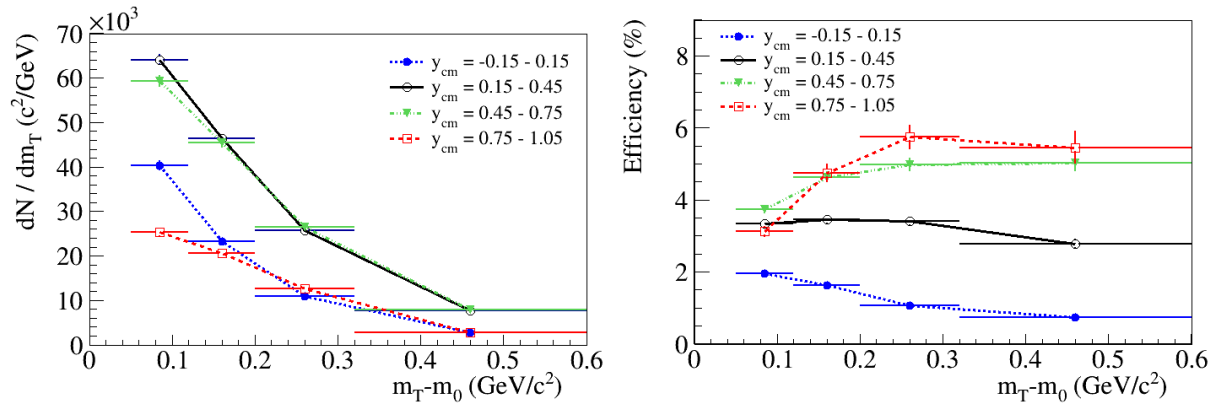

Figure 10: (Left) Λ hyperon raw yields versus transverse mass for 4 intervals of rapidity; (right) total reconstruction efficiency versus m_T for 4 rapidity intervals. Lines are drawn to guide the eye.
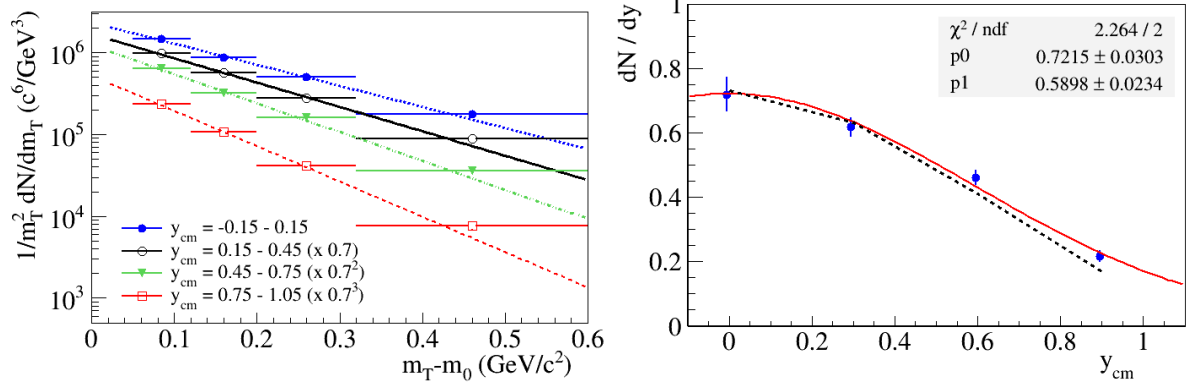
Figure 11: (Left) transverse mass distributions of Λ hyperons for 4 rapidity bins fitted to the Boltzman expression. The effective temperatures T_{eff} obtained are: 170±8, 144±4, 126±3 and 105±4 MeV with the highest value corresponding to the lowest rapidity interval. (Right) Λ hyperon rapidity spectrum fitted to the gaussian with zero mean (full line) compared with a prediction from the DCM-SMM generator (dashed line).

4.2 K_S^0 meson

The same procedure was applied to reconstruct K_S^0 decays. The obtained results are presented in Figs. 12 - 16.

Figure 12 illustrates the steps to reconstruct the decay curve from the raw lifetime distribution and the estimated total reconstruction efficiency. Figures 13 and 14 show how the efficiency - corrected m_T spectra are built and used to obtain the decay curve after proper integration, while Figs. 15 and 16 demonstrate the steps to reconstruct the rapidity spectrum. Figure 16 also includes the model prediction from the DCM-SMM generator which seems to overestimate currently measured K_S^0 multiplicity (not corrected for the trigger efficiency) by a factor of $\sim$1.6 similarly to what was observed at the STAR experiment in Au+Au fixed-target run at the beam kinetic energy of 2.91A GeV [19] in comparison with a prediction of the Monte Carlo event generator UrQMD [20].
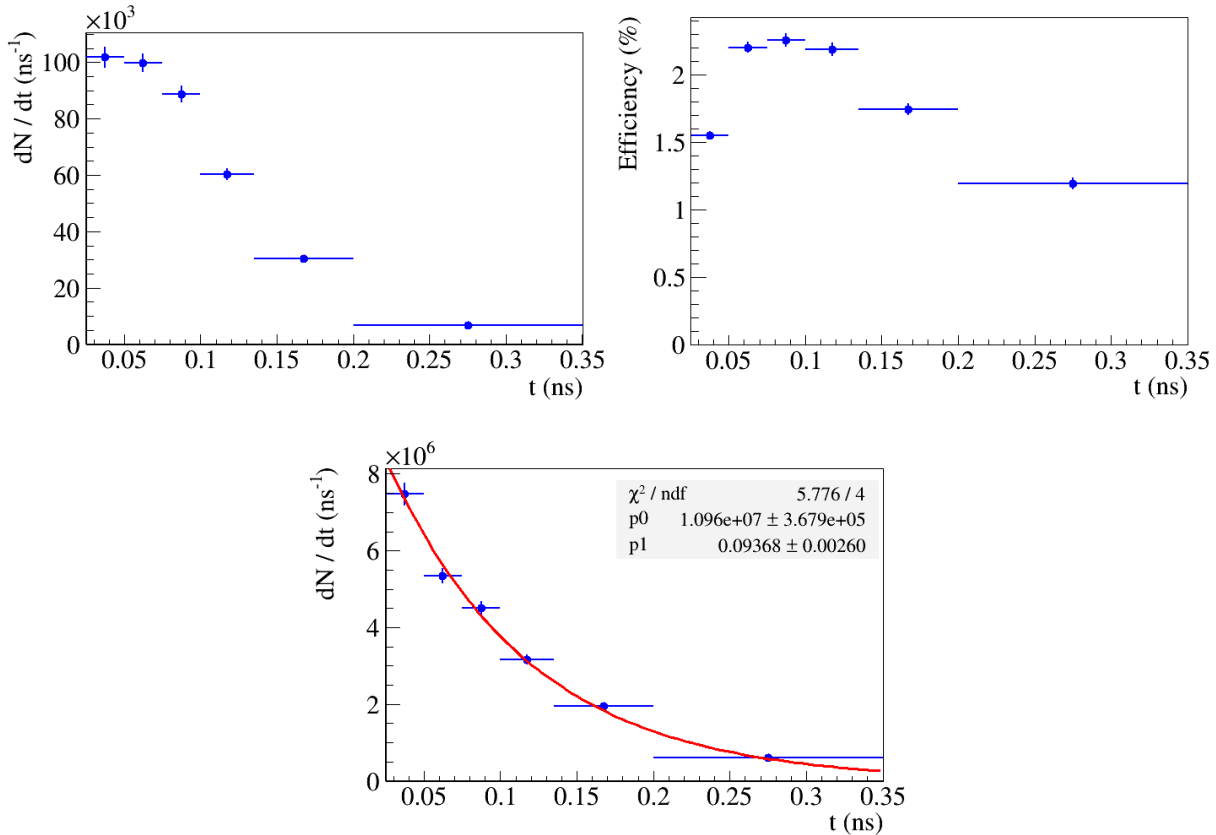

Figure 12: (Left) reconstructed K_S^0 meson yield versus lifetime; (right) total K_S^0 meson efficiency obtained from Monte Carlo simulation; (bottom) K_S^0 meson lifetime distribution corrected for efficiency, fitted to the decay curve (2) with $p1$ table value of 0.089 ns.
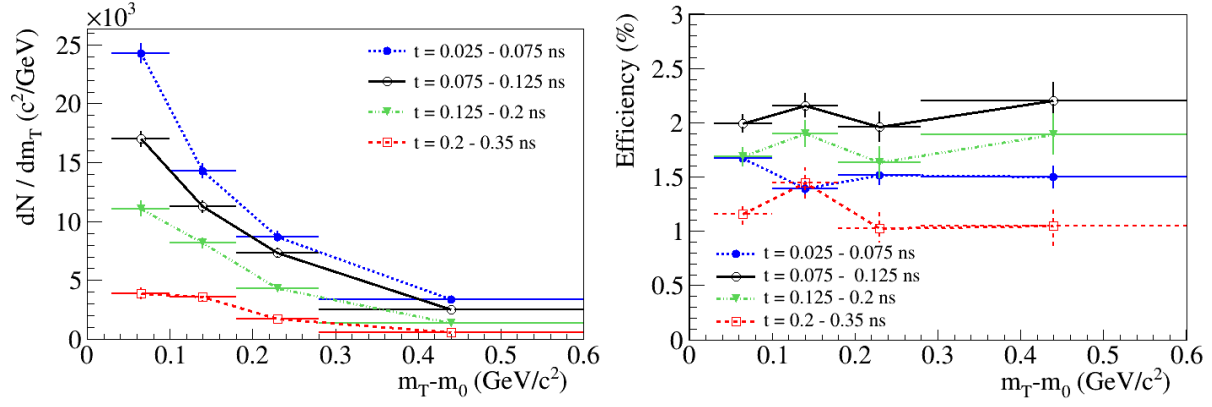
Figure 13: (Left) K_S^0 meson raw yields versus transverse mass for 4 intervals of lifetime; (right) total reconstruction efficiency. Lines are drawn to guide the eye.
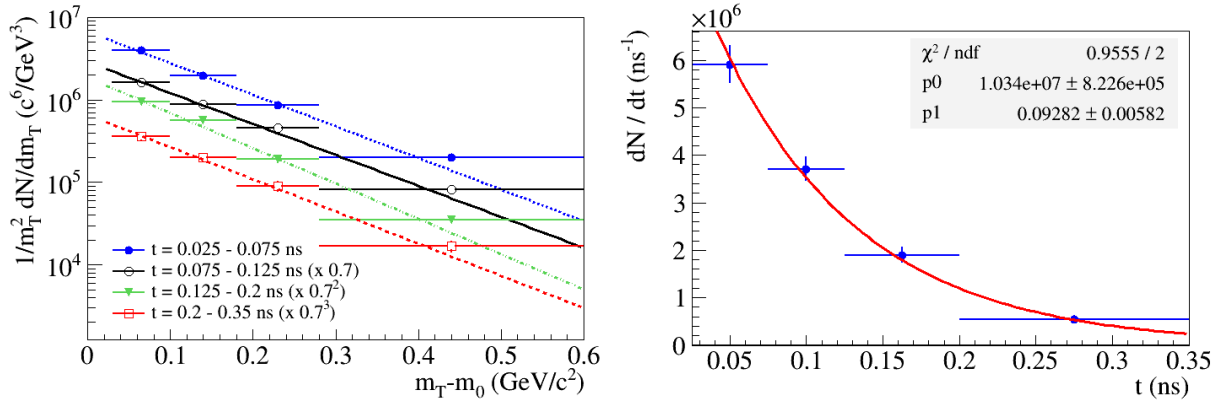

Figure 14: (Left) transverse mass distributions of K_S^0 mesons for 4 lifetime bins fitted to the Boltzman expression (4). The effective temperatures T_{eff} obtained are: 113±3, 116±3, 101±4 and 111±8 MeV for the lifetime bins of 0.025 - 0.075, 0.075 - 0.125, 0.125 - 0.2 and 0.2 - 0.35 ns, respectively. (Right) reconstructed decay curve from integrated m_T spectra fitted to the expression (2).
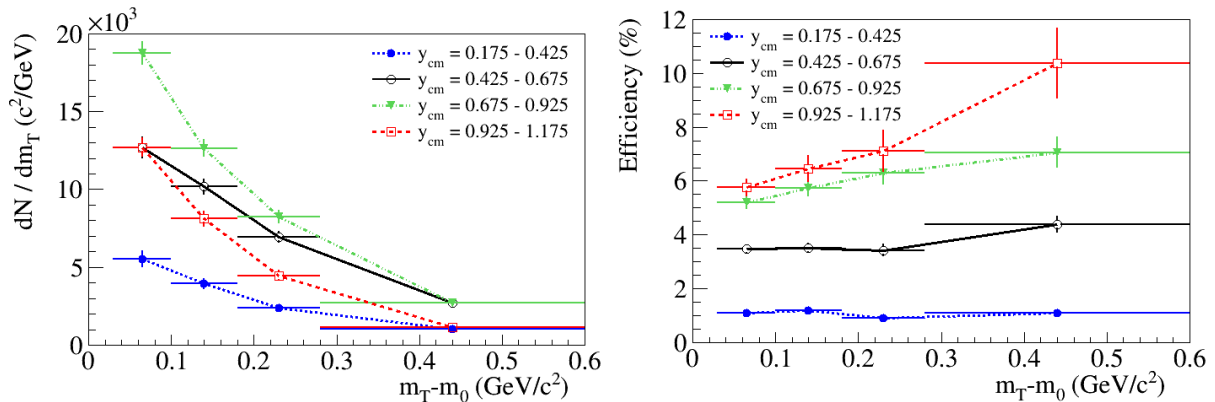

Figure 15: (Left) K_S^0 meson raw yields versus transverse mass for 4 intervals of rapidity; (right) total reconstruction efficiency. Lines are draw to guide the eye.
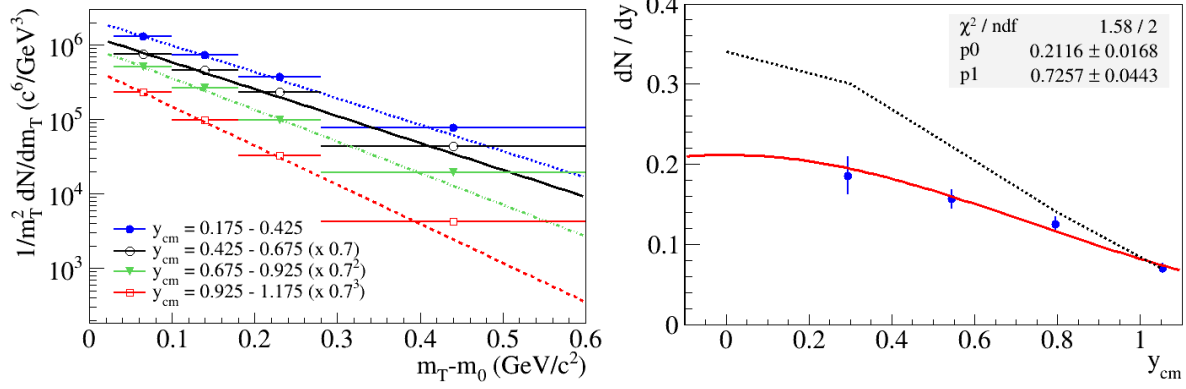
Figure 16: (Left) Transverse mass distributions of K_S^0 mesons for 4 rapidity bins fitted to the Boltz-man expression (4). The effective temperatures T_{eff} obtained are: 122±7, 120±4, 102±3 and 83±3 MeV with the highest value corresponding to the lowest rapidity interval. (Right) K_S^0 me-son rapidity spectrum fitted to the gaussian with zero mean value (full line) and compared with a prediction from the DCM-SMM generator (dashed line).

5 Summary and future developments

The procedures for reconstruction of strange particle decays at the BM@N experiment have been described and their performance demonstrated. As a validation step of the developed and implemented reconstruction approach, some very preliminary results on strange particle production in Xe+CsI interactions at 3.8A GeV beam energy have been presented. It should be stressed here that the physics performance plots and distributions should not be considered as physics analysis results and are presented solely to better illustrate the reconstruction performance and to indicate the direction of the future activity, which is the actual physics analysis with much higher event statistics and proper consideration of several important items such as trigger efficiency, collision centrality, estimation of systematic effects, etc.

References

[1] P. Senger, "Studies of dense nuclear matter at NICA", [arXiv:2005.13856 [nucl-ex]]

[2] P. Senger, "Heavy-Ion Collisions at FAIR-NICA Energies", Particles **4**, no.2, 214 (2021)

[3] P. Senger, "Review of the BM@N Physics and Upgrade Program", Phys. Part. Nucl. **52**, no.4, 506 (2021)

[4] P. Senger, "Probing Dense Nuclear Matter in the Laboratory: Experiments at FAIR and NICA", Universe **7**, no.6, 171 (2021)

[5] V. Friese, "Prospects for the study of baryon-rich matter at new facilities", PoS **CORFU2018**, 186 (2019)

[6] M. Kapishin, "Studies of baryonic matter at the BM@N experiment (JINR)", Nucl. Phys. A **982**, 967 (2019)

[7] M. Kapishin *et al.*, "Production of hyperons, strange mesons and search for hypernuclei in interactions of carbon, argon and krypton beams in the BM@N experiment", Phys. Part. Nucl. **52**, 710 (2021)

[8] K. Redlich, A. Tounsi, "Strangeness enhancement and energy dependence in heavy ion collisions", Eur. Phys. J. C **24**, 589 (2002)

[9] S. Afanasiev *et al.* [BM@N Collaboration], "The BM@N spectrometer at the NICA accelerator complex", Nucl. Instrum. Meth. A **1065**, 169532 (2024)

[10] D. Zinchenko, E. Nikonov, A. Zinchenko, R. Zinchenko, "Development of the Vector Finder toolkit for track reconstruction in the BM@N experiment", Phys. Part. Nucl. Lett. **21**, no.3, 544 (2024)

[11] D. Zinchenko, A. Zinchenko, R. Zinchenko, E. Nikonov, "Development of a Vector Finder toolkit for track reconstruction at NICA experiments: current status and future prospects", Phys. Part. Nucl. **55**, no.4, 811 (2024)

[12] P. Batyuk, K. Gertsenberger, S. Merts, O. Rogachevsky, "The BmnRoot framework for experimental data processing in the BM@N experiment at NICA", EPJ Web. Conf. **214**, 05027 (2019)

[13] R. Luchsinger, Ch. Grab, "Vertex reconstruction by means of the method of Kalman filter", Comput. Phys. Commun. **76**, 263 (1993)

[14] S. Gorbunov, I. Kisel, "Reconstruction of decayed particles based on the Kalman filter", CBM-SOFT-note-2007-003. 7 May 2007. Available online: `https://www.star.bnl.gov/~bouchet/KFParticle/DOC-2007-May-14-1.pdf` (accessed on 15 November 2024).

[15] A. Zinchenko *et al.*, "A Monte Carlo Study of Hyperon Production with the MPD and BM@N Experiments at NICA", Particles **6**, no.2, 485 (2023)

[16] V. Kolesnikov, D. Suvarieva, V. Vasendina, A. Zinchenko, "Optimization of Techniques for Λ Hyperon Measurement at MPD/NICA," Phys. Part. Nucl. **55**, no.4, 827 (2024)

[17] M. Baznat, A. Botvina, G. Musulmanbekov, V. Toneev, V. Zhezher, "Monte-Carlo Generator of Heavy Ion Collisions DCM-SMM", Phys. Part. Nucl. Lett. **17**, no.3, 303 (2020)

[18] G. Agakishiev *et al.* [HADES Collaboration], "Hyperon production in Ar+KCl collisions at 1.76A GeV", Eur. Phys. J. A **47**, 21 (2011)

[19] M. I. Abdulhamid *et al.* [STAR Collaboration], "Strangeness production in $\sqrt{s_{\mathrm{NN}}}$ = 3 GeV Au+Au collisions at RHIC," JHEP **10**, 139 (2024)

[20] M. Bleicher *et al.*, "Relativistic hadron hadron collisions in the ultrarelativistic quantum molecular dynamics model", J. Phys. G **25**, 1859 (1999)